Materials properties of magnesium and calcium hydroxides from first-principles calculations

A. Pishtshev,[1] S. Zh. Karazhanov,[2,*] and M. Klopov[3]

[1]*Institute of Physics, University of Tartu, 51014 Tartu, Estonia*
[2]*Department for Solar Energy, Institute for Energy Technology, NO-2027 Kjeller, Norway*
[3]*Department of Physics, Tallinn University of Technology, 19086 Tallinn, Estonia*

(Dated: April 7, 2014)

This work presents a study of ground state properties, electronic structure, dielectric and optical properties of magnesium and calcium hydroxides $X(OH)2$ (X= Mg and Ca) within PBE-GGA and range-separated hybrid functional schemes as well as by using GW approximation. The relevant HSE06 hybrid functional mixing parameters were determined from a self-consistent adjustment to the electronic dielectric constant ϵ_∞. It was shown that the overall performance of our adaptation of the HSE06 functional via implementation of the modified amount of the Fock exchange is nearly best for the ground state properties as compared to other relevant HF and DFT methods. Structural stability of the crystalline $X(OH)2$ hydroxides has been considered in static and dynamic aspects. The most important factors describing the bonding situation have been investigated, and a crystal-chemical integrity of the hydroxides has been analyzed. From electronic structure studies it was found that both materials are direct band gap insulators. Predictions for the fundamental band gaps were shown to be in the range of 7.7-8.3 eV for $Mg(OH)_2$ and 7.3-7.6 eV for $Ca(OH)_2$. The origin of the conduction and valence band states near the band edges has been studied in terms of orbital and site projected density of states as well as by comparison with the X-ray photoelectron spectroscopy measurements. It was shown that effective masses of carriers at the Γ-point in vicinity of the band extreme are strongly anisotropic and for the electrons are similar to those in the ZnO crystal. Optical properties of the bulk $X(OH)2$ hydroxides have been investigated in terms of the real and imaginary parts of the optical dielectric function calculated in GW approximation. Electronic character of anisotropy of optical properties has been clarified. On the base of the obtained results the potential of applicability of the $Mg(OH)_2$ and $Ca(OH)_2$ crystalline hydroxides in semiconductor device engineering and optoelectronics has been analyzed.

PACS numbers: 31.15.A-; 71.20.Ps; 63.70.+h
Keywords: magnesium hydroxide, brucite, calcium hydroxide, lime, crystal structure, electronic structure, chemical bonding, work function, optical properties

I. INTRODUCTION

Alkaline earth metal hydroxides $X(OH)2$ (X=Mg, Ca) represent a fine example of multifunctional compounds having a widest range of technological and industrial applications. The elements compromising $X(OH)2$ are widely available, low cost, and non-toxic. Hydrogen (H) and oxygen (O) are the most abundant elements in the universe. Because of the possibility of synthesis by inexpensive and green method, these materials can be chemically tuned with predesigned functional properties and, therefore, they hold very good promises for future applications, e.g., biomedicine, electronic device, solar energy, gas sensing, etc. For instance, along with calcium containing binary oxides and carbonates, portlandite $Ca(OH)_2$ is one of the most key inorganic materials in lime industries. In addition to the pivotal uses in building and engineering fields its functional properties are widely involved in a variety of applications; the primers range from water treatment,[1] dental therapy,[2] enhancement of electronic connectivity, reduction of the trapping/detrapping events, and suppression of charge recombination in the semiconductorelectrolyte interface of the dye-sensitized solar cells.[3] Brucite $Mg(OH)_2$ has demonstrated similar effectiveness in waste water treatment[4–7] and and high antibacterial efficiency against several tested bacterial strains.[8] There is an interesting experience of employing $Mg(OH)_2$ as a precursor for magnesium oxide refractory ceramics,[9] or as a flame retardant in various polymer compositions and smoke suppressants.[9–11]

Note that the most of applications of the hydroxides are based mainly on the employing of their chemical properties that envisage the constituent metal cations and hydroxyl anions as principal participants in the target chemical transformations. At the same time, exploring the possibilities of unique physics of the bulk hydroxides at the microscopic (electronic) level has been difficult for a long time. However, in recent years special attention was given to investigations related to the crystal growth design and preparations of crystalline hydroxide thin films.[3,12–19] This allowed researches to carry out a number of experimental studies which have suggested several effective ways of examining whether the hydroxides can become an integral part of solid-state electronic devices via the relevant exploration of their electronic properties.[20] In particular, it was successfully demonstrated for the case of the CuInSe[12,13] and dye-sensitized[3,21–23] composite solar cells that $Mg(OH)_2$ films may be easily incorporated in such devices as a buffer

layer in order to accommodate differences of lattice constants and band offsets between two different materials. Another emerging application was offered on the base of $Mg(OH)_2$ films doped with certain amounts of C atoms.[19] The primary goal was to create a new type of rare-earth metal free transparent and conducting films in which the host material belonging to a group of wide-gap insulators is transparent to the visible light. The resulting $Mg(OH)_2$:C films have shown unusual behavior under a light illumination of the wavelength range of 380 nm - 780 nm, namely a regular transmission of $\sim 90\%$ accompanied with a considerably high electrical conductivity of ~ 167 S/cm.[19]

Thus, the possible usage of the $X(OH)2$ hydroxides in solid-state electronics requires firm knowledge of their fundamental physical properties, which is an important task at the moment. Systematic experimental studies of structural, morphological, and vibrational properties of $X(OH)2$ have been previously performed in a number of works (see, e.g., Refs. 24–31). From the theoretical side, in the focus were mainly structural, vibrational and chemical properties.[32,33] Recent studies on the electronic structure were undertaken primarily to understand novel opto-electronic properties of $Mg(OH)_2$:C films.[34]

Among unique features the hydroxides commonly exhibit the layered structure seems to be the major factor that not only governs, at the macroscopic level, different properties of these materials, but also should develop effective relations between the existing chemical interactions. The suggestion that these interactions, being active simultaneously, are connected via the simplest functional group – OH^- hydroxyl anion, directs essential attention to the issues of an interplay between ionicity and covalency such as (i) understanding how covalency is involved within the charge transfer process, and (ii) identifying how it affects the basic electronic properties inherent in the rigid ionic crystalline systems. A straight involvement of covalency in the activation of the electronic subsystem follows directly from an analysis of the Honjo *et al.* experiments[19] on $Mg(OH)_2$:C films, whereas the interplay of the ionic and covalent interactions can be seen from experimental studies[12,13,23] that demonstrate the possibilities of accommodation of lattice constants and band offsets in composite solar cells with a buffer layer of $Mg(OH)_2$. The present work thus aims to give a first-principles outlook that quantifies structure-bonding-properties relationships for the $X(OH)2$ hydroxides in terms of DFT calculations with emphasis on studying structural stability, features of electronic structure, mechanical and optical properties. Because of the absence of the detail theoretical studies that could serve as a guide for the electron subsystem, we will focus on the points that are principally important for the knowledge of key parameters and mechanisms underlying the specific properties of the hydroxides and that can contribute to the development of semiconductor devices using these compounds as the host or secondary materials, i.e. what can provide an excellent starting point for the present or future explorations. Since little information is presented about real electronic structure of the hydroxides in scientific literature, the other problem addressed in our work has a rather academic character; recent progress in numerical DFT methods has allowed us via performing accurate DFT calculations to update significantly theoretical description of the fundamental electronic and optical properties of these compounds.

II. METHODS AND COMPUTATIONAL DETAILS

A. Methodological aspects

For ionic-covalent materials usually one starts electronic structures calculations that can output theoretical predictions of the important properties such as band gap values, the band picture, density of states by using traditional local density approximation (LDA) or semilocal generalized gradient approximation (GGA) to DFT. For improvement of the description of the electronic states built of Kohn-Sham virtual orbitals one can decide between two possibilities: either to use computationally accessible hybrid functionals, which deal with a specified fraction of the Fock exchange, or to employ the powerful theoretical tool such as the many-body Hedin's GW approximation (GWA).[35] As both ways give the great adjustment of the results obtained on the base of LDA and GGA functionals, in the present work we apply numerical procedures based on HSE06 hybrid functional[36–38] within the frameworks of which we describe the crystal structure and determine electronic and dielectric properties of the $X(OH)2$ hydroxides.

Since exchange effects (as an integral part of electron-electron interactions) appear to be especially significant in the wide-gap ion-covalent materials, the problem of how to describe the electronic structure in terms of single-particle states depends on inherent availability of the hybrid functional to model effectively the full $(x, x^{'})$- and ω-dependent electron interactions in terms of the exact Fock exchange. Working inside of first-principles electronic structure methods, a useful way of making such treatment is consideration of the non-local hybrid functional as an approximation to the true electron self-energy $\Sigma(x, x^{'}; \omega)$, which provides theoretical constructs that map efficiently to typical elements of the hybrid functional like as follows:[39,40] $\Sigma(x, x^{'}; \omega)$ is projected into the direct sum of two principal terms – the first corresponds to a statically screened non-local exchange in which the amount of the exchange is driven by the inverse electronic dielectric constant ϵ_{∞}^{-1} and the second is identified with the static and local part of the hybrid functional; the quasi-particle equation followed from such construction corresponds to the generalized Kohn-Sham equation that can be self-consistently solved for a hybrid functional. The main benefit that was originally gained in this context is that by including

the fraction a (the mixing coefficient) of the Fock exchange as ϵ_∞^{-1} into the exchange correlation (xc) potential $V_{xc} = aV_x^F + (1-a)V_x^{GGA} + V_c^{GGA}$ it provided rationale for the efficient accounting for the corresponding non-local **r**-dependencies, yielding thus a single-particle description of electronic states for periodic systems, such as ion-covalent insulating systems, much more accurate as compared to results recorded by conventional DFT-based calculations on the base of LDA or GGA. Moreover, the proper solutions of the generalized Kohn-Sham equation with a hybrid functional such as the eigenvectors and eigenvalues can be further used as a first starting point to evaluate various material properties of the physical system.

From a pragmatic point of view, note that while hybrid functional based approach may be subjected to some discussion concerning the certain amount of the exchange contribution in the functional, which appears to be system-dependent parameter, this issue is quite well amenable to first-principles procedure that, with the goal of clearing that bottleneck, can evaluate a physical range of values of a via ϵ_∞^{-1} (Refs.39,41–44) without relying on experimental input. To this end, the present study starts with a preliminary series of calculations aimed to ascertain the relevant fraction of the Fock exchange a that will be consistently utilized further as a material-specific parameter in the structure of the HSE06 hybrid DFT functional. Detail considerations concerning numerical and theoretical treatment of the mixing parameter a in the HSE06 hybrid functional in terms of ϵ_∞^{-1} can be found in Refs. [44,45]. Based on that, we could also add that due to strong inequality $r_{TF} >> (2/\mu)$ universally common to ion-covalent insulators such parametrization is generally safe for tuning the optimal a; here r_{TF} is the Thomas-Fermi screening length and μ characterizes the range separation in the HSE06 hybrid functional. Next, with this background the subsequent series of calculations is directed to evaluate accurately electronic structure and materials properties of the hydroxides.

One can also add that such methodology of variable exchange implementation in the HSE06 functional is quite general within the framework of one parameter hybrid approximation and, therefore, can be applicable without any special renewing for representation of the ground state of the other materials having the same brucite-type structure such as transition metals hydroxides $Co(OH)_2$ and $Ni(OH)_2$. We are planning to report in the near future the results of our calculations on these materials.

B. Computational details

For all periodic DFT calculations we have employed Vienna *ab initio* simulation package (VASP)[46] together with the potential projector augmented-wave (PAW) method.[47–49] To ensure data accuracy and clarity, proper convergence tests with respect to the cutoff energy for the expansion of the wave function and Brillouin zone sampling have been performed. In all our calculations a large plane-wave basis set with 800 eV cutoff, and a Γ point centered $8 \times 8 \times 8$ mesh for the **k**-point sampling, have been chosen. GW-versions of PAW-PBE pseudopotentials were adopted with $2p^6 3s^2$, $3s^2 3p^6 4s^2 3d^0$, $2s^2 2p^4$, and $1s^1$ valence electron configurations for Mg, Ca, O and H atoms, respectively. The calculations have been made within the Perdew-Burke-Ernzerhof (PBE)[50] GGA exchange-correlation functional and HSE06 hybrid functional with a modified portion of the Fock exchange. The numerical procedure for evaluation of the mixing coefficient a via the equation $a = \epsilon_\infty^{-1}$ was carried out in terms of iterative improvement as follows: At first, theoretical modeling of the lattice relaxation and dielectric properties was made at the PBE-GGA ground state: once the optimization was completed, the elements of the macroscopic dielectric matrix were numerically evaluated using density functional perturbation theory as implemented in VASP.[51] Taking these elements as initial guess for a via ϵ_∞^{-1} ($\epsilon_\infty = (2\epsilon_\infty^{xx} + \epsilon_\infty^{zz})/3$), next was calculation of improvements to the macroscopic dielectric matrix by using this guess as "argument" in the modified HSE06 hybrid functional. At this stage the iterative loop was closed. Calculated in this way, the components of ϵ_∞ along with the corresponding mixing coefficients a adopted in the present work are shown in Table I. Note that on the both stages of these calculations the local field (LF) effects have been taken into account.

Table I: Calculated values of the macroscopic dielectric matrix for $Mg(OH)_2$ and $Ca(OH)_2$. The last column shows the fraction of the Fock exchange values of the mixing coefficients a adopted in the properties calculations. All energies are given in eV.

Compound	PBE	HSE06m	a
$Mg(OH)_2$	$\epsilon_\infty^{xx} = 2.63$	$\epsilon_\infty^{xx} = 2.34$	
	$\epsilon_\infty^{zz} = 2.60$	$\epsilon_\infty^{zz} = 2.38$	
	$\epsilon_\infty = 2.62$	$\epsilon_\infty = 2.35$	0.425
$Ca(OH)_2$	$\epsilon_\infty^{xx} = 2.73$	$\epsilon_\infty^{xx} = 2.36$	
	$\epsilon_\infty^{zz} = 2.52$	$\epsilon_\infty^{zz} = 2.26$	
	$\epsilon_\infty = 2.66$	$\epsilon_\infty = 2.33$	0.429

Effective masses of electrons (m_e) in the conduction band (CB) and holes (m_h) in the valence band (VB) along the high symmetry $\Gamma \to M, \Gamma \to A$ and $\Gamma \to K$ directions were estimated via a parabolic approximation for the band edge energies $E(\mathbf{k})$; the numerical values of the second order derivatives have been obtained from the (nonrelativistic) hybrid DFT calculations by performing polynomial fitting of the curves $E(\mathbf{k})$.

A theoretical way for computing correctly the optical properties was chosen according to the currently wide accepted, useful strategy[52–55] that utilizes hybrid DFT functional wave functions as a starting point for performing GW procedures. The real and imaginary parts of the optical dielectric function $\epsilon(\omega)$ were numerically evaluated in GW approximation as implemented in VASP[56–59] by summing interband transitions from occupied to un-

occupied states for energies much higher than those of phonons. More details about the optical calculations are discussed in Refs. [60,61].

III. RESULTS

A. Equilibrium properties

Both magnesium and calcium hydroxides belong to a class of layered crystalline systems: they crystallize in a trigonal structure (space group $P\bar{3}m1$, no. 164) with one f.u. per the unit cell62–65. As compared with the other bivalent metal hydroxides, no other polymorphs of $Mg(OH)_2$ and $Ca(OH)_2$ have been reported in literature.[66,67]

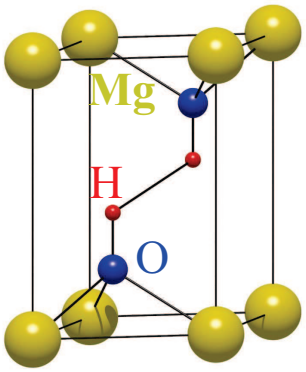

Figure 1: Schematic presentation of unit cell of $X(OH)2$ (X=Mg and Ca). Mg and Ca atoms are sketched by the large grey color balls.

In the brucite structure (Fig. 1) each X^{2+} metal cation is octahedrally surrounded by six O^{2-} anions, each of which in turn is tetrahedrally connected with one H^+, forming OH^- complex, and with three X^{2+}. Such interplay of two different coordinations allows one to represent an ideal equilibrium lattice structure of a brucite-type hydroxide in terms of layers of $XO6$ octahedra parallel to the axis c and a hexagonal close packing of the hydroxyl anions in the **ab**-plane.[67]

Full geometrical optimization of the lattice structure with respect to the unit cell size and internal positions has been performed within the frameworks of the standard PBE-GGA and the modified HSE06 functionals. The results listed in Table II for the lattice constants, atomic coordinates, and bond lengths and angles show clearly the role of the exact exchange contribution – the relaxed zero-pressure lattice parameters and the selected interatomic local distances not only agree well with the experimental data, but also they are in general more accurate than those from PBE-GGA optimization. Moreover, the comparison with results of previous studies performed within the Hartree-Fock formalism (HF) and some representative DFT based methods shows that our adaptation of the HSE06 functional via tuning the mixing coefficient has a profoundly positive effect on the structural optimization of the $X(OH)2$ hydroxides. For instance, the remarkable shortening of the O−H bonding distances as compared with the GGA results is convincing proof that covalency effects are more completely treated within the hybrid functional with the modified weight of the exact exchange. This fact means that the utilization of the exact exchange reduces the self-interaction and delocalization errors in the description of O−H bonding. Comparing the calculated equilibrium volumes with those experimentally determined one can also see that the increase of the Fock exchange significantly reduces the corresponding deviations from the experimental data: ∼1.38% (2.32%) and ∼0.51% (0.58%) for $Mg(OH)_2$ and $Ca(OH)_2$, respectively.

B. Stability aspects

The principal issue related to the structural stability of the $X(OH)2$ hydroxides is connected with results of the recent computer simulations[71] which have suggested that at least for the magnesium hydroxide the P$\bar{3}$m1 symmetry unit cell may be less convenient as compared with the hypothetical low-symmetry P$\bar{3}$ $\sqrt{3}\times\sqrt{3}\times1$ supercell. Let us show from the computational point of view that if one starts from the relaxed high-symmetry ground state, one can give two compelling arguments in favor of stability of the experimentally determined P$\bar{3}$m1 geometry. The first represents a standard test of the positivity criterion for the squares of harmonic frequencies at $\mathbf{q} = 0$ (i.e. corresponds to dynamical stability). Table III and Table IV summarize data of this test in terms of the Raman and infrared spectra of the optical vibrational modes obtained in the harmonic approximation along with the available experimental data and the previous theoretical calculations.

The second argument deals with a demonstration of mechanical (elastic or macroscopic) stability. In Table V six linearly independent elastic constants[77,78] calculated for the $X(OH)2$ crystals are presented, five of them are compared with experimental data. Firstly, we indicate here that components of the elasticity tensor evaluated on the base of the relaxed P$\bar{3}$m1 equilibrium geometry are well consistent with those predicted by experiment.[79–81] Secondly, one can see that elastic stability criteria of the trigonal system[82,83] certainly hold, i.e. $(C_{11}+C_{12})C_{33} - 2C_{13}^2 > 0$, $C_{66}C_{44} - C_{14}^2 > 0$, $C_{66} > 0$. It is therefore obvious that the crystalline form of the P$\bar{3}$m1 space symmetry is the elastically stable structure of $X(OH)2$ hydroxides.

As seen from characteristics of aggregate properties (Tables V) and VI) both materials show moderate strength properties; albeit $Mg(OH)_2$ exhibits much better hardness (≈ 1.8 times harder than $Ca(OH)_2$ [121]) and stiffness. They are quite well compressible ($\nu_V = 0.20$ and 0.25), more resistant to volume change over shape change ($B_V/G_V > 1$), more inclined to brittle frac-

Table II: Comparison of experimental and calculated geometries (unit-cell dimensions, volumes, ion cell positions, and interionic distances).

		Expt		PBE	HSE06	HF	PW91	B3LYP
$Mg(OH)_2$		Ref. [62][a]	Ref. [63]		($a = 0.425$)	Refs. [68,69]	Refs. [68,69]	Refs. [68,69]
$P\bar{3}m1$	a(Å)=	3.145	3.150	3.189	3.126	3.148	3.179	3.167
	c(Å)=	4.740	4.770	4.773	4.730	5.263	4.717	4.854
	V($Å^3$)=	40.60	40.99	42.02	40.04	45.2	41.3	42.2
	c/a=	1.507	1.514	1.497	1.513	1.672	1.484	1.533
O, H (2d):								
1/3 2/3 z	z(O) =	0.2194	0.2203	0.2183	0.2183	0.1972	0.2210	0.2143
	z(H) =	0.4195	0.4130	0.4214	0.4191	0.3757	0.4271	0.4125
Distances (Å):	Mg−O	2.093	2.100	2.115	2.079	2.093	2.111	2.104
	O−H	0.953	0.958	0.969	0.950	0.940	0.972	0.962
	H−H	1.966	1.969		1.960	2.239	1.960	2.016
	∡M−O−H		120°		119.8°	119.7°	119.6°	119.6°
$Ca(OH)_2$		Ref. [64][b]	Ref. [65]		($a = 0.429$)	Ref. [27]		Ref. [27,70]
$P\bar{3}m1$	a(Å)=	3.589	3.592	3.612	3.575	3.666		3.620
	c(Å)=	4.911	4.906	4.942	4.923	5.185		5.010
	V($Å^3$)=	54.78	54.82	55.85	54.50			56.80
	c/a=	1.368	1.366	1.368	1.377	1.414		1.384
O, H (2d):								
1/3 2/3 z	z(O) =	0.2341	0.2341	0.2316	0.2306			
	z(H) =	0.4285	0.4248	0.4280	0.4240			
Distances (Å):	Ca−O	2.370	2.371	2.379	2.356	2.401		2.402
	O−H	0.955	0.936	0.972	0.952	0.933		0.965
	H−H	2.188	2.201		2.196	2.399		2.190
	∡Ca−O−H	119°	119°		118.8°			

[a] At 70 K.
[b] At room temperature.

Table III: Raman spectra of zone center harmonic optical vibrations (cm^{-1}) of the $X(OH)2$ hydroxides as compared to experimental data and other calculations.

Mode	This Work	MD	B3LYP	Expt	
	(PAW-PBE)	Ref. [72]	Ref. [70]	Ref. [73]	Ref. [29]
		$Mg(OH)_2$			
E_g	269	279	272	280	280
A_{1g}	413	444	457	443	444
E_g	807	720	780	725	725
A_{1g}	3411	3655	3859	3652	–
		Ref. [72]	Ref. [70]	Ref. [73]	Ref. [74]
		$Ca(OH)_2$			
E_g	238	254	252	254	260
A_{1g}	352	358	371	357	359
E_g	678	676	702	680	684
A_{1g}	3704	3619	3836	3620	3620

Table IV: Infrared spectra of zone center optical vibrations (cm^{-1}) of the $X(OH)2$ hydroxides as compared to experimental data and other calculations.

Mode	This Work	MD	B3LYP	Expt	
	(PAW-PBE)	Ref. [72]	Ref. [70]	Ref. [29]	Ref. [73]
		$Mg(OH)_2$			
E_u	356	373	352	365	361
E_u	416	461	479	415	416
A_{2u}	438	562	490	455	461
A_{2u}	3710	3695	3859	–	3688
		$Ca(OH)_2$			
E_u	266	312	289	304	287
E_u	361	392	441	392	373
A_{2u}	339	418	363	415	334
A_{2u}	3725	3646	3849	–	3640
				3644[a]	3651[b]

[a] Reference [75].
[b] Reference [76].

ture, and exhibit large degrees of the acoustic anisotropy ($A = 0.32$ and 0.37, respectively). Due to significant smallness of the off-diagonal constant C_{14} compared to the other independent components of the elasticity tensor, the both compounds can be practically related to a class of transversely isotropic elastic materials.[91] However, being matched the macroscopic elastic constants show a noticeable decrease for $Ca(OH)_2$ with the corresponding volume increase (Table II). In structural aspect, it means that if one compare infrared harmonic frequencies given in Table IV, and the elasticity tensor components of Table V, such as C_{44} and C_{66}, one can observe the following two facts: (i) the certain "softening" tendency appearing once the metal cation is fully substituted from Mg to Ca, and (ii) a noticeable fall of the elastic effective characteristics as shown in Tables V) and VI. By

Table V: Linearly independent components of the elasticity tensor in GPa for the $X(OH)2$ hydroxides (PAW-PBE) as compared to experimental data. The elastic anisotropy factor (A) represented in terms of the ratio $A = C_{33}/C_{11}$ describes the anisotropy of the compressional field. In the last column, the combination of C_{11} and C_{12} in terms of $C_{66} = (1/2)(C_{11} - C_{12})$ is added.

Comp.	C_{11}	C_{12}	C_{13}	C_{33}	C_{44}	C_{14}	A	C_{66}
$Mg(OH)_2$								
This work	156.3	45.0	10.1	50.4	21.8	0.2	0.32	55.7
Expt.79	156.7	44.4	12.0	46.3	21.7		0.30	56.2
Expt.80	159.0	43.3	11.1	49.5	22.8		0.31	57.9
$Ca(OH)_2$								
This work	102.7	31.6	8.1	37.6	9.4	0.5	0.37	35.6
Expt. 81	99.3	36.2	(29.7)[a]	32.6	9.8		0.33	31.6

[a]This value is considered in Ref. 81 as unreliable.

Table VI: Results for the macroscopic effective elastic constants of the $X(OH)2$ hydroxides represented in terms of the Voigt-Reuss-Hill scheme[84] as compared with experimental data. The bulk (B), shear (G) and Young's (E) modulus are in GPa, ν denotes Poissons ratio, and β_c/β_a describes the ratio of linear compressibility along the c- and a axises, respectively. The estimates are given for the case of an orthotropic solid since in calculations we omitted C_{14} due to its significant smallness.

Comp.	B	G	E	ν	B/G	β_c/β_a
$Mg(OH)_2$						
This work	46.4	35.4	84.7	0.20	1.31	4.5
Expt.[a]	51.0(±4.0)					
Expt.[b]	54.3(±1.5)					5.20(±0.50)
Expt.[c]	47.0(±5.0)					2.0
$Ca(OH)_2$						
This work	32.7	19.9	49.5	0.25	1.65	4.0
Expt.[d]	37.8(±1.8)					3.20(±0.40)
Expt.[e]	38.3(±1.1)					2.95(±0.25)
Expt.[f]	34.2(±1.4)					
Expt.[g]	30.8(±2.3)					

[a] Shock compression measurements.[85]
[b] X ray diffraction measurements at 300 K.[86]
[c] Neutron powder diffraction measurements.[87]
[d] X ray diffraction measurements at room temperature.[88]
[e] Determined from powder neutron diffraction data by using lagrangian finite strain theory.[89]
[f] Determined from powder neutron diffraction data by using the Birch-Murnaghan equation of state.[89]
[g] Determined from powder X-ray diffraction data by using a third order finite strain fit.[90]

comparison the similar "softness" takes also place for the bulk modulus of CaO against that of MgO.[89] Moreover, the exchange of Mg−O connection for the Ca−O one is accompanied by considerable decrease of the hexagonal ratio c/a from 1.51 to 1.37. In chemical bonding sense it means that once Ca^{2+} cation succeeds in accommodation into a lattice site of the bulk $Ca(OH)_2$, becoming ready for electrostatic forces promotion within the cationic framework, then it not necessarily distort the local structural environment, increasing the strain energy, but instead it tends to relieve the local stresses via a partial softening of central ionic connections as compared with $Mg(OH)_2$, hence lowering the elastic properties. In this context, due to a significant drop in the shear elastic component C_{44} relative to $Mg(OH)_2$ (by a factor of 2.3), $Ca(OH)_2$ when subjected an external force might be considered in terms of the stability condition $C_{66}C_{44} - C_{14}^2 \simeq C_{66}C_{44} > 0$ for searching a mechanical instability against the shear connected with the induced softness of one of the transverse acoustic modes. Thus, the cation replace from Mg for Ca in the hydroxide family changes unfavorably the energetics of the host hexagonal packed structure, making $Ca(OH)_2$ to be a soft solid, so that it is not surprisingly that there are only two alkaline earth hydroxides of brucite-type, $Mg(OH)_2$ and $Ca(OH)_2$, that retain the $P\bar{3}m1$ symmetry under ambient conditions.

In addition to examination of structural stability the chemical stability of $Mg(OH)_2$ and $Ca(OH)_2$ can be analyzed in terms of the heat of formation (ΔH_f^0). Generally, ΔH_f^0 being the leading term of Gibbs free energy can be calculated as the enthalpy difference between a compound and its constituent elements in their most stable states according to the theoretical decomposition pathway $X(OH)2 \rightarrow X + O_2 + H_2$. In terms of energies the latter can be described by the following equation:

$$\Delta H_f^0 = E[X(OH)2] - E[X] - E[O_2] - E[H_2]$$

for X=Mg and Ca. Here $E[...]$ is the total energy corresponding to ground state of $X(OH)2$, X, O_2, and H_2, respectively. The results of evaluations of ΔH_f^0 along with experimental values are summarized in Table VII. The calculated heats of formation coincide well with the experimental data – the theoretical evaluation of energies required to decompose these compounds gives values that are approximately 2.6% and 3.7% larger than those provided by experiment. These values fall within the typical range related to ion-covalent insulators; for comparison, the heats of formation for most common crystalline hydroxides[92] are on the order of −4.3 - −10.2 eV (with the exception of −2.48 eV related to thallium hydroxide).

Table VII: Heats of formation for $Mg(OH)_2$ and $Ca(OH)_2$ (eV).

Compound	Theory[a]	Expt.[b]	Diffr.(%)
$Mg(OH)_2$	−9.84	−9.59	2.6
$Ca(OH)_2$	−10.60	−10.22	3.7

[a]This work.
[b]Reference [12].

C. Chemical bonding aspects

Exactly what could be said about the overall chemical bonding picture in an inorganic ion-covalent system depends on information of how and to what extent ionic connections and covalency appear and coexist in the system. Characterization of activities and functional roles of the leading chemical interactions can be made in terms of electron partitioning schemes. The most important factors describing the bonding situation in the hydroxides are presented in: (i) Table VIII which summarizes calculated values of the Bader effective and Born dynamic charges, and (ii) Figs. 2, 3 and 4, which visualize ELF valence electrons distributions.

As seen from analysis of the Bader charges of Table VIII, the effect of a charge transfer is that divalent Mg^{2+} is almost fully oxidized; divalent Ca^{2+} is slightly less oxidized, however due to larger electronegativity difference with respect to oxygen it remains in ionic state as well. Hydrogen demonstrates also the positive oxidation state of about +0.56 and +0.52 as compared to more positive magnesium (+1.79) and calcium (+1.65). Interesting topological feature that follows from the partition of the unit cell space is that valence electrons of the oxygens controls about 78% and 67% of the cell volume in $Mg(OH)_2$ and $Ca(OH)_2$, respectively. Certainly, this fact gives the direct qualitative indication that the main contribution to electronic responses of these materials will belong to the oxygen valence orbitals.

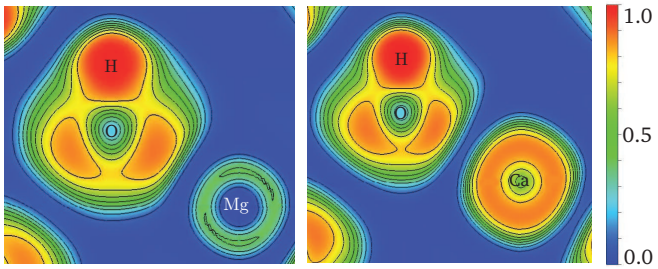

Figure 2: Representation of the valence ELF for the three-body structural Mg−O−H (left) and Ca−O−H (right) units in (110) cut plane. ELF values increase from blue to red.

In the context of the overall bonding situation our results suggest that the three-body structural $X-O-H$ block, which is build up with the central oxygen acting as a major oxidizer, is principal to provide a common chemical stability in terms of stable arrangement of chemical interactions upon formation of the hydroxide. From Fig. 2 one can see two direct evidences of such "structuring", namely a loss of electron density (small ELF values) in the nearby area about the X^{2+} cation, and a denser distribution (higher ELF values) at the other end, which corresponds to a large valence electrons gathering in the spatial region between the central oxygen and adjacent hydrogen ions. By referring to the Bader charge analysis (Table VIII) the latter clearly indicates that two valence electrons, the one donated by the oxygen and the other – by the hydrogen, reside with a higher probability in this area causing the covalent bond formation along c axis. Therefore, the key feature of bonding in the $X-O-H$ unit is that the one-electron oxidation processes on each half-side lead to an inequivalency of chemical bonds on the left and right of the central oxygen. In other words, to balance electron-poor and electron-reach areas the valence electrons move very differently across bonding distances, so that the electron density differences are such that the most positive charge lies on the longest equilibrium $X-O$ bond distance providing the closed shell configuration of the metal cation and ionic bonding with the oxygen, while the less positive hydrogen is strongly bonded to the same oxygen by the vertical covalent connection. It is thus become clear the particular role of the oxygen anion in the hydroxides which in fact is that not only to generate the cations due to electron transfer but also to build up a bridging site that is responsible for a structural stabilization via maintaining two different chemical interactions with its electropositive partners within the $X-O-H$ unit. Thus, both Mg^{2+} and Ca^{2+} form rigid ordered cationic networks that by electrostatic interactions are connected with hydroxyl anions. Due to weakness of effects of the metal-ligand overlap (i.e. hybridization of relevant local orbitals related to valence electrons) admixture of covalency along the Mg−O, Ca−O connections remains quite sparse. At the macroscopic level, this conclusion is well supported by the magnitude of the ratio of the $Mg(OH)_2$ and $Ca(OH)_2$ bulk moduli (Table VI), 1.42, which is only 12.5% larger than the theoretical prediction of 1.26. The latter, using the data of Tables II and VIII, can be obtained on the base of the bulk modulus-volume relationship[94] found to be hold for ionic compounds such as oxides, halides, *etc.*

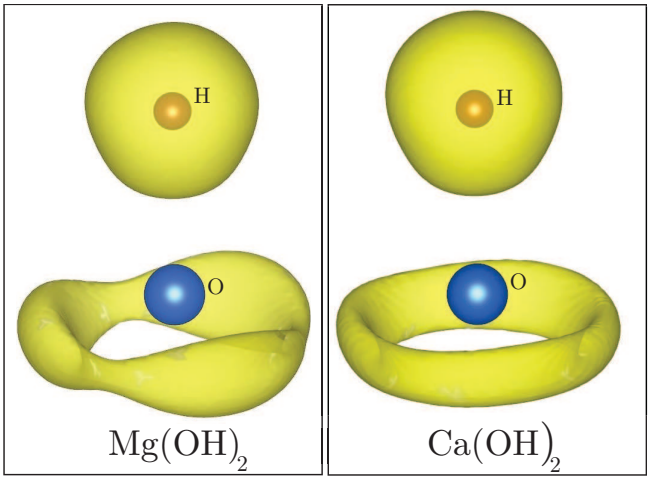

Figure 3: Valence ELF isosurfaces at ELF= 0.87 for the hydroxyl anion in $Mg(OH)_2$ (left) and $Ca(OH)_2$ (right).

Regarding the ligand subsystem, shown in Fig. 3 is a visualization of the electronic density of the OH^- an-

Table VIII: Charge characteristics related to the host ions in $Mg(OH)_2$ and $Ca(OH)_2$ (in units of $|e|$). The Pauling electronegativities are taken from[93] δ_O describes the electronegativity difference with respect to O. The quantities $Q_B(M)$ denote the Bader effective charges calculated from electronic densities. Z^*_{ij} is the matrix of the Born effective charges. The quantity $\bar{Z}^*(M) = (1/3)(Z^*_{xx}(M) + Z^*_{yy}(M) + Z^*_{zz}(M))$ represents the average of the principal values over crystal axes.

$Mg(OH)_2$	Mg	O	H	OH^-
δ_O	2.13	0	1.24	–
$Q_B(M)$	+1.79	−1.45	+0.56	−0.89
$Z^*_{ij}(M)$	$\begin{pmatrix} +2.07 & 0 & 0 \\ 0 & +2.07 & 0 \\ 0 & 0 & +1.92 \end{pmatrix}$	$\begin{pmatrix} -1.46 & 0 & 0 \\ 0 & -1.46 & 0 \\ 0 & 0 & -1.29 \end{pmatrix}$	$\begin{pmatrix} +0.42 & 0 & 0 \\ 0 & +0.42 & 0 \\ 0 & 0 & +0.32 \end{pmatrix}$	$\begin{pmatrix} -1.04 & 0 & 0 \\ 0 & -1.04 & 0 \\ 0 & 0 & -0.97 \end{pmatrix}$
$\bar{Z}^*(M)$	+2.02	−1.40	+0.39	−1.02
$Ca(OH)_2$	Ca	O	H	OH^-
δ_O	2.44	0	1.24	–
$Q_B(M)$	+1.65	−1.34	+0.52	−0.82
$Z^*_{ij}(M)$	$\begin{pmatrix} +2.34 & 0 & 0 \\ 0 & +2.34 & 0 \\ 0 & 0 & +1.96 \end{pmatrix}$	$\begin{pmatrix} -1.56 & 0 & 0 \\ 0 & -1.56 & 0 \\ 0 & 0 & -1.26 \end{pmatrix}$	$\begin{pmatrix} +0.38 & 0 & 0 \\ 0 & +0.38 & 0 \\ 0 & 0 & +0.26 \end{pmatrix}$	$\begin{pmatrix} -1.18 & 0 & 0 \\ 0 & -1.18 & 0 \\ 0 & 0 & -1.00 \end{pmatrix}$
$\bar{Z}^*(M)$	+2.21	−1.46	+0.34	−1.12

ion represented in terms of the valence ELF isosurface at ELF= 0.87. It is well seen two regions (in the vertical and planar directions) of shared-electron interactions that form distributions of localized electrons with different shapes. The strong covalent contribution into O−H bonding caused by the deep overlapping of the valence orbitals of oxygen and hydrogen is established along c axis. Due to a vertical (oriented) deformation of the localized electronic cloud from sphericity this covalency has partially polar character.

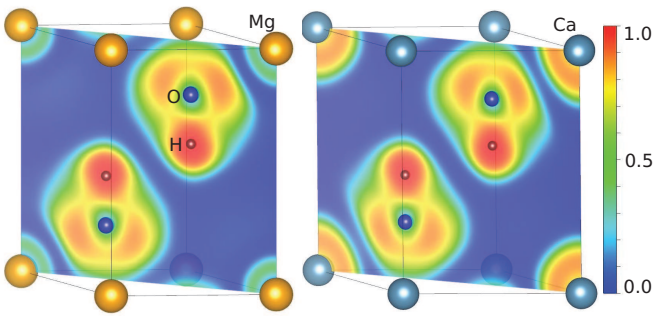

Figure 4: A cut (110) plane through the valence ELF of $Mg(OH)_2$ and $Ca(OH)_2$. ELF values increase from blue to red. O and H atoms are sketched by the red and light grey color balls, respectively.

A cut (110) plane of the ELF topology drawn in Fig. 4 for the both hydroxides allows us to reveal in a total absence of hydrogen-bonded areas in terms of unshared electron connections like O−H · · · O or O−H · · · H−O. Moreover, a canceling of hydrogen bonding is directly strengthen by the opposite sign of the polarity of the covalency at which the overall electronic density tends to be pushed to the inner part of O−H bonding region, i.e the resulted electronic shift appears to be especially unfavorable in the sense of hydrogen bonding activation.

The next important point to be discussed in the context of the $X - O - H$ unit is the dynamic coupling of the relevant lattice distortions with a macroscopic electric field. Generally, this interaction, as an ion-covalent system specific bonding component associated with the purely dynamic part of the charge transfer, is fundamental for the structural stability of polarized insulating crystals such as displacive ferroelectrics.[95–98] Because of the spatial non-uniformity inherent to the distribution of the electronic density in $X-O-H$, it is important to understand what kind of movements in this structure – changes in an ionic environment or distortions of electronic shells caused by mixing with long-wavelength optical vibrations – is principal in treating the macroscopic crystal polarizability and effects of the local field. In this context, analysis of the components of the tensor of the Born effective charges is of great importance because their enhanced values with respect to some reference (nominal) ionic values serve as confirmation for many-body electronic polarization effects that contribute to ionic dipole polarization.[98,99] As shown in Table VIII the components of the dynamic charges are not high; with the exception of Ca^{2+} for which there is a modest influence of hybridization effects featuring the empty $3d$ orbitals, the other ions demonstrate values that are either closed to or even less than their nominal ionicities. Thus, the role of direct distortions of the valence electron charge density, i.e. processes caused by mixing electronic movements with long-wavelength optical vibrations, is not expected to be considerable in the $X(OH)2$ hydroxides. An additional test for the lattice-driven contribution to macroscopic polarization can be made in terms of the ionic ($\mathbf{P}^{(i)}(0)$) and electronic ($\mathbf{P}^{(e)}(0)$) amplitudes of polarization associated with the polar long-wavelength optical mode. A simple analytical estimate[98] $\mathbf{P}^{(i)}(0)/\mathbf{P}^{(e)}(0) = (\epsilon_\infty - 1)/3$, deduced within the Born model,[100] shows that the lattice polarization is about 2.2 times larger than the electronic one. This is an important indicator, because it demon-

strates that the ionic (lattice) polarization contribute in a larger degree to the internal macroscopic field of the hydroxides.

One of the main features of $Mg(OH)_2$ and $Ca(OH)_2$ is that chemically they are versatile solid hydroxides as under the action of heat they can be dehydrated into simple oxides and water,[67]
$Mg(OH)_2 \xrightarrow{550\,K} MgO + H_2O$ and
$Ca(OH)_2 \xrightarrow{400\,K} CaO + H_2O$,
and vice versa – synthesized within the backward reaction involving the use of MgO or CaO as a solid component. Proton-driven thermal mechanism of these reactions[101] can be represented as follows:[102]
$H_2O_{dissolved} + O^{2-}_{structure} \leftrightarrow (OH^- + OH^-)_{structure}$.
Let us show how being based on the above given bonding picture one can gain insight into microscopic nature of hydration/dehydration chemical transformations. To this end we focus on the equilibrium geometry of the hydroxides and take into account three relevant facts, namely, the reversibility of the decomposition $\leftarrow -> $ composition pathways, instability of O^{2-} in the free state as well as no evidence of existence of the alkaline earth metal cations in the free state. Then one can consider that the transformations are mainly achieved by structural rearrangements of key functional elements such as Mg^{2+}, Ca^{2+} and O^{2-} ions. Since linking of these ions gives rise to Mg−O, Ca−O ionic bonds, which are formed by the resulting charge-transfer due to large electronegativity between Mg, Ca on one hand, and O on the other hand, the direct bounding of water molecules to metal centers becomes impossible. A representative example of importance of electrostatic interactions is given by comparison of the Mg−O, Ca−O bond lengths of Table II with the sums of the corresponding single-bond ionic radii: $r(Mg^{2+})+r(O^{2-}) = 2.10$ and $r(Ca^{2+}) + r(O^{2-}) = 2.38$ Å for $Mg(OH)_2$ and $Ca(OH)_2$, respectively ($r(Mg^{2+}) = 0.86$ Å, $r(Ca^{2+}) = 1.14$ Å, $r(O^{2-}) = 1.24$ Å).[93] In other words, the distribution of valence electron density inside Mg−O or Ca−O environment is setting in such a manner as mainly to support and exactly optimize ionic connections in the lattice carcase of the given compounds, so that the possible formation of monohydrates occurs to be generally avoided. Correspondingly, in order to increase the susceptibility towards ionic bonding, the water (during reaction) is incorporated into the new crystalline structure via deprotonation process accompanied by activation of the O−H bond. The resulting formation of the OH^- anions, which as it is well-known[103] is a very poor leaving group, provides a smooth establishment of the relevant relationships of a standard ionic character. Correspondingly, upon heating the dehydration of the hydroxides happens in reverse order: the OH^- anion is protonated to give an intermediate oxonium which facilitates the formation of the much better leaving group, a water molecule. At the same time, as follows from low and moderate values of the macroscopic elastic constants (Table VI), the optimization of the ionic connections of 'metal cation'–'hydroxyl anion' type does not have to be resulted in strong bonding as compared with the typical oxides of alkaline earth metals. As we have seen from the bonding analysis of the $X-O-H$ unit the total strength of the long-range $X-O$ Coulomb interactions is directly driven by the participating of the divalent bridging oxygen anion in the covalent bond with the hydrogen. Given that 2/3 of the atoms in the bulk hydroxide belong to a hydroxyl anion, this provides the possibility for the thermal dehydration via the canceling of the short-range O−H forces within the $X-O-H$ unit followed by the simple oxide formation and the release of the molecular water leaving the system. In this context, since the unit cell parameters such as a and c lattice vectors increase noticeably as cation is fully substituted from Mg to Ca (Table II), it becomes clear that an increase in volume makes the dehydration temperature of $Ca(OH)_2$ smaller than that of $Mg(OH)_2$.

D. Electronic structure, effective masses, and density of states

1. *Band picture*

In this section 5 we continue to describe the bonding situation via an analysis of the band structure and the density of states (DOS). Figure 5 presents the calculated band structure indicating that the both $X(OH)2$ are direct band gap materials with the VB maximum and the CB minimum located at the Γ-point.

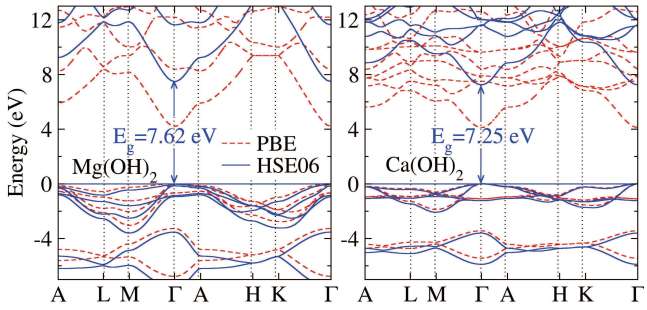

Figure 5: Band structure of $X(OH)2$ calculated within both PBE-GGA and HSE06m hybrid functional schemes. The Fermi level is set to zero.

The energies of the valence and conduction bands closest to the fundamental gap along with the symmetry classification of the electronic states in the key high-symmetry points of the first Brillouin zone (BZ) are summarized in Table IX. It is interesting to note that despite the fact that GGA underestimates the band gap energy, comparison of the curvatures at the VB maximum and CB minimum in the increased scale of Fig. 5 indicates that both the modified HSE06 hybrid and PBE semi-local functional determine a similar character of dispersions around conduction and valence band edges (Fig. 6).

Table IX: Energy states of the valence and conduction bands closest to the fundamental gap and their symmetry classification in the high-symmetry points of the first BZ. The zero energy corresponds to the top of the valence band.

Band	$Mg(OH)_2$					
	L	M	Γ	A	H	K
E_{v5}	$-5.73(A_g+Au+B_u)$	$-4.72(A_g+A_u+B_u)$	$-3.41(A_{1g}+A_{2u})$	$-5.119(A_{1g}+A_{2u})$	$-5.629(A_1+A_2+E)$	$-5.19(A_1+A2+E)$
E_{v4}	$-2.36(A_g+A_u+B_u)$	$-3.41(A_g+A_u+B_u)$	$-0.79(E_u)$	$-0.639(E_u)$	$-2.589(A_1+E)$	$-3.11(A_1+A2+E)$
E_{v3}	$-2.03(A_g+A_u+B_u)$	$-2.33(A_g+A_u+B_u)$	$-0.79(E_u)$	$-0.639(E_u)$	$-1.848(E)$	$-2.16(E)$
E_{v2}	$-1.14(B_u)$	$-1.45(B_u)$	$0(E_u)$	$-0.158(E_u)$	$-1.478(A_1+A_2+E)$	$-2.16(E)$
E_{v1}	$-0.68(B_u)$	$-0.32(B_u)$	$0(E_u)$	$-0.158(E_u)$	$-1.478(A_1+A_2+E)$	$-1.17(E)$
E_{c1}	$12.06(A_g+A_u+B_u)$	$12.06(A_g+A_u+B_u)$	$7.70(A_{1g}+A_{2u})$	$9.431(A_{1g}+A_{2u})$	$13.401(A_1+A_2+E)$	$13.35(E)$
E_{c2}	$12.35(A_g+A_u+B_u)$	$12.90(A_g+A_u+B_u)$	$11.84(A_{1g}+A_{2u})$	$11.990(A_{1g}+A_{2u})$	$13.401(A_1+A_2+E)$	$13.36(A_1+A_2+E)$
Band	$Ca(OH)_2$					
	L	M	Γ	A	H	K
E_{v5}	$-4.53(A_g+A_u+B_u)$	$-4.55(A_g+A_u)$	$-3.61(A_{1g}+A_{2u})$	$-4.70(A_{1g}+A_{2u})$	$-4.71(A_1+A_2+E)$	$-4.61(A_1+A2+E)$
E_{v4}	$-1.42(A_g+A_u+B_u)$	$-2.04(A_g+A_u+B_u)$	$-1.21(E_u)$	$-1.04(E_u)$	$-1.14(A_1+A_2+E)$	$-1.72(A_1+A2+E)$
E_{v3}	$-1.03(B_u)$	$-0.92(A_g+A_u+B_u)$	$-1.21(E_u)$	$-1.04(E_u)$	$-1.14(A_1+A_2+E)$	$-1.29(E)$
E_{v2}	$-1.01(A_g+A_U+B_u)$	$-0.75(B_u)$	$0(E_u)$	$-0.20(E_u)$	$-1.14(A_1+A_2+E)$	$-1.29(E)$
E_{v1}	$-0.38(B_u)$	$-0.66(B_u)$	$0(E_u)$	$-0.20(E_u)$	$-0.86(A_1+A_2+E)$	$-0.24(A_2+E)$
E_{c1}	$10.55(A_g+A_u+B_u)$	$9.57(A_g+A_u+B_u)$	$7.33(A_{1g}+A_{2u})$	$8.89(A_{1g}+A_{2u})$	$11.86(A_1+A_2+E)$	$10.37(E)$
E_{c2}	$11.38(A_g+A_u+A_u)$	$10.88(A_g+A_u+B_u)$	$11.56(A_{1g}+A_{2u})$	$10.84(A_{1g}+A_{2u})$	$11.86(A_1+A_2+E)$	$10.82(A_1+A_2+E)$

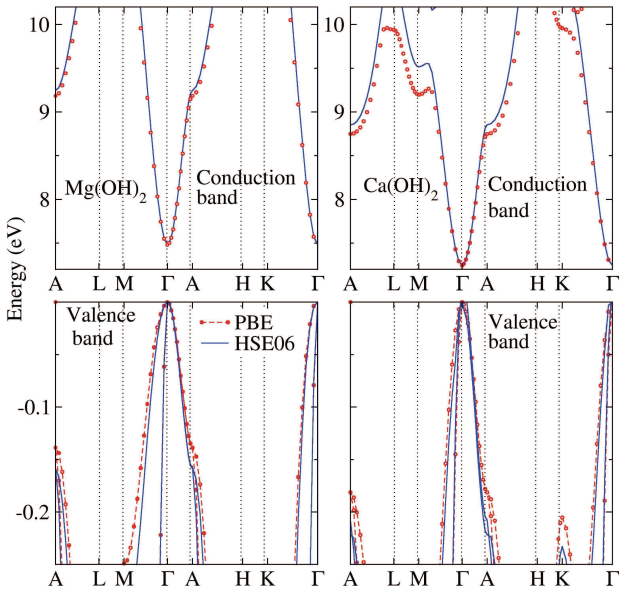

Figure 6: Fine structure at the Γ-point of the VB and CB states in $X(OH)2$ calculated within PBE and HSE06 functional schemes.

As is visible from Fig. 5, the bottommost CB states are much more dispersive than the topmost VB states. In particular, the VB E_{v1}, E_{v2} in the Γ-A (Δ) direction, and upper split branch of E_{v1} in the Γ-M (Σ) direction is almost flat opposite to the lowest CB E_{c1} which is classically dispersive. It means that when the material is externally influenced, this feature could be the source of the principal differences related to mobilities of the band carriers, as, for example, the localization of a non-equilibrium heavy hole may facilitate in the VB. In order to confirm this point we have estimated effective masses of conduction electrons (m_c) and holes (m_{1h}, m_{2h}) along the high-symmetry $\Gamma \rightarrow M, \Gamma \rightarrow A$ and $\Gamma \rightarrow K$ directions, which are presented in Table X.

Since the band dispersion around the conduction and valence band extreme calculation within PAW-PBE and HSE06 are almost the same, we have estimated the effective masses using the band structure calculated by HSE06. The results show strong anisotropy of the hole effective masses in VB of $X(OH)2$. It is also seen that along several symmetry axes holes are significantly heavier than electrons and hence more localizable. Analysis based on Figs. 2, 3 and 4 has shown that the microscopic reason of this difference is that the valence electrons tend to be tightly bound within OH^- anions what in turn results in almost flat structure of the valence band states. At lower energies the electron effective masses in the CB of $Mg(OH)_2$ are similar to those of $Ca(OH)_2$ and close to the value of 0.13 m_0 observed in ZnO (Ref. [106]). It indicates that one can expect mobility of carriers in the CB and, consequently, electrical conductivity of $X(OH)2$ to be in the limits of that of ZnO. Another interesting feature of the CB structure is that at the bottom it consists of two neighbor states that are split in energy >3.1 eV. At the macroscopic level this may provide a possibility of effective application of the material with the following property: if an impurity forms shallow donor level in the band gap and possesses high solubility, then the material could still be transparent to the incident light.

Table X: Effective masses of electrons in CB and holes in two nearest VB (in units of the free-electron mass m_0) for $Mg(OH)_2$ and $Ca(OH)_2$ estimated from band structure calculations within HSE06.

	$Mg(OH)_2$	$Ca(OH)_2$	ZnO[a]	ZnO[b]
$m_e(\Gamma \rightarrow M)$	0.13	0.18		0.23
$m_e(\Gamma \rightarrow A)$	0.18	0.20	0.24	0.21
$m_e(\Gamma \rightarrow K)$	0.20	0.28		
$m_{1h}(\Gamma \rightarrow M)$	3.06	0.44	0.59	2.74
$m_{1h}(\Gamma \rightarrow A)$	5.25	0.50	0.59	0.54
$m_{1h}(\Gamma \rightarrow K)$	4.17	0.30	0.59	3.03
$m_{2h}(\Gamma \rightarrow M)$	0.13	0.22	0.55	0.55
$m_{2h}(\Gamma \rightarrow A)$	3.14	3.10	0.31	0.27
$m_{2h}(\Gamma \rightarrow K)$	0.14	0.34	0.55	1.12

[a]Experiment from Ref. [104].
[b]Theory from Ref. [105]. FP-LMTO method.

2. Density of states

Figure 7 presents orbital and site projected density of states (PDOS) calculated at relaxed lattice geometries by using the HSE06 functionals with the mixing parameters of Table I. It is seen that the relative ratio of *s*-, *p*-, and *d*-related contributions in PDOS significantly differ. By donating two valence *s*-electrons to fill the $2p$ oxygen shell the empty *s*-type orbitals of Mg^{2+} or Ca^{2+} are readily hybridized with the empty *s*-type orbitals of O^{2-}. However their mixture which according to Figure 7 is responsible for the lowest states of the CB exhibits much lower intensities as compared with the highest occupied valence band states.

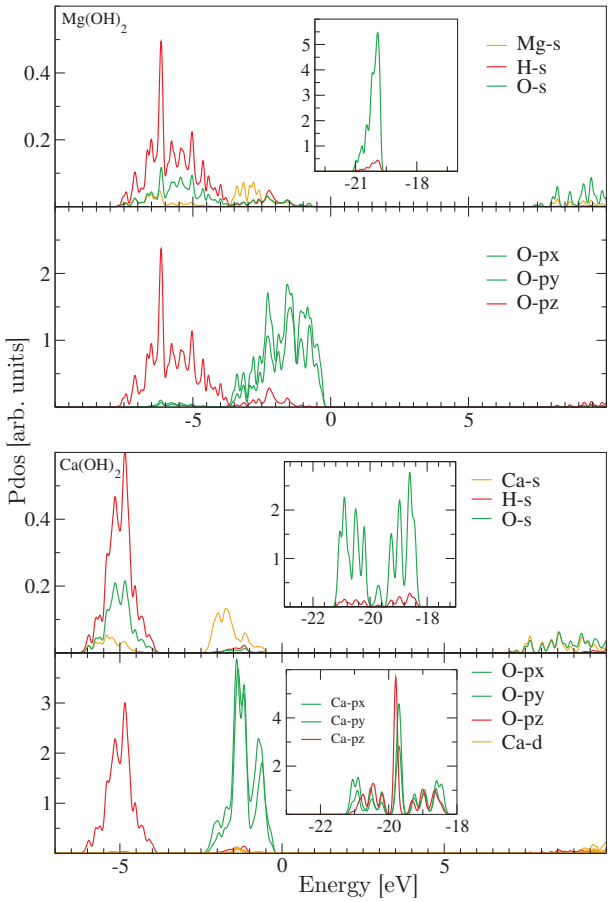

Figure 7: Orbital and site projected density of states for $X(OH)2$.

The upper part of the VB, which lies in the energy ranges between $-8 \div 0$ eV ($Mg(OH)_2$) and $-6 \div 0$ eV ($Ca(OH)_2$), consists of the p and s states of O^{2-}, the s states of H^+, and the s states of the metal cation. The deeper part of the VB in $Mg(OH)_2$ is represented by the narrow DOS pick centered at -20.1 eV which corresponds to contributions of the oxygen *s* core states. Comparison with experiment has shown that the both parts of the calculated VB agrees very well with X-ray photoelectron spectra (XPS) measurements[107] performed for $Mg(OH)_2$ (Fig. 8).

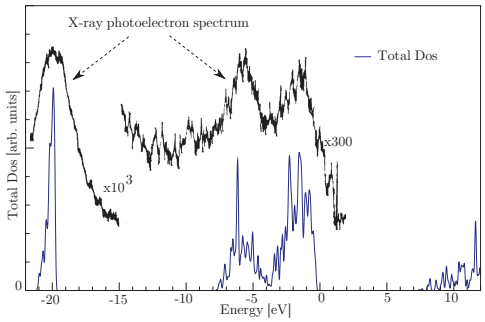

Figure 8: Total density of states obtained within the PBE-GGA and HSE06 hybrid functional schemes as compared with the experimentally measured X-ray photoelectron spectrum.[107] The Fermi level is set to zero.

The central feature of the electronic spectra at the Γ point is that highest occupied *p*-type orbitals of oxygen split into twofold degenerate $(2p_x, 2p_y)$ and non-degenerate $2p_z$ electronic states (bands E_{v1}, E_{v2} and E_{v3}, respectively), as indicated in Fig. 7 and Table IX, giving rise to two different oxygen valence subbands. Correspondingly, the minimum band gap of 7.70 and 7.33 eV for $Mg(OH_2)$ and $Ca(OH_2)$, respectively, is associated with transitions from the top of O^{2-} $2p_x, 2p_y$ states. Due to the strong sp_z hybridization between H and O orbitals the occupied O $2p_z$ electronic states are shifted (especially in the case of $Ca(OH)_2$) into depth of the electronic spectra. The full substitution of Mg for Ca adds the following visible differences affecting the common structure of PDOS: first, the presence of the multiplet structure of Ca^{2+} $3d$-related states (Fig. 7) in the CB, which above the fundamental absorption preedge show considerable weights in DOS, secondly, a contraction of all oxygen $2p$ subbands and hydrogen *s* band in the VB, and lastly, more complex character of the deeper part of the VB – being aligned in DOS with maximum at -19.7 eV it consists of the mixture of the calcium *p* and the oxygen *s* core states. The later gives rise to the additional metal-nonmetal sp^3 covalent bonding that is complimentary to the main electrostatic interactions in CaO_6 octahedra.

Thus, the splitting of an angular character of the oxygen electronic states in the hydroxides is associated with the different roles the valence electrons play in chemical interactions. The electrons supplied by the alkaline earth metal are transferred via charge-transfer channel to provide a classical ionic bond – an electrostatic interaction of the anionic hydroxyl group with the metal cation in xy plane. The electron contributed by the hydrogen atom remain located inside the OH^- ion to be employed in mostly covalent O−H bond along c axis. By these valence electron density redistribution processes covalent bonding is embedded into the elemental framing of ionic structure changing the angular character of the highest occupied *p*-type electronic states.

3. Work function

The electronic potential of the hydroxides can be highlighted via theoretical analysis of the work function of electrons (WF), knowledge of which allows one to understand a wide range of physical phenomena sensitive to surface properties such as thermionic emission, photoemission, catalysis, etc.[108] From physical side, since the induced electron ejection (removing) is a charge transfer process, the magnitude of WF can be estimated in terms of electron transfer[109] via the change in the energies of the relevant electronic states, namely as the difference between the Fermi (E_F) and vacuum (V) levels: $W = V - E_F$. The vacuum level is defined here as the electrostatic potential outside the surface of a solid. Correspondingly, the computational method for V is based on the macroscopic technique,[110] while the Fermi level E_F inside the material can be obtained self-consistently from the DFT calculations.[110–112]

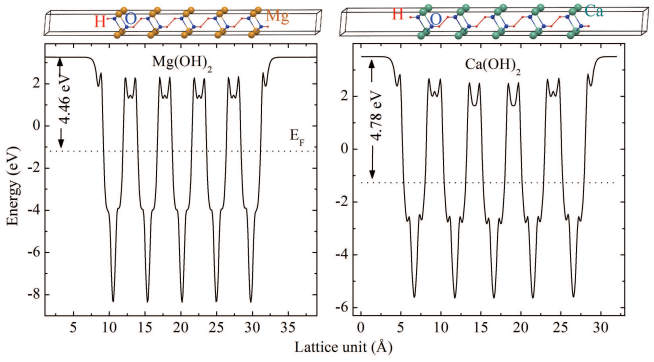

Figure 9: The electron potential energy across $X(OH)2$ and vacuum. Fermi level E_F is plotted by dotted line.

We have carried out our calculations of WF for the hydroxides along the [001] direction using the model of a 1×1×5 slab surrounded by the vacuum (Fig. 9). The results are listed in Table XI. Comparison reveals that

Table XI: The calculated values of WF (eV) for $Mg(OH)_2$ and $Ca(OH)_2$ as compared with relevant materials.

$Mg(OH)_2$	$Ca(OH)_2$	MgO[a]	CaO[a]	CaO/Mo(001)[b]	ZnO[c]
4.46	4.78	3.1–4.4	1.6–2.7	4.0	4.7

[a]Ref. [113].
[b]Ref. [114].
[c]Ref. [115].

the transition from the binary XO oxides to the related $X(OH)2$ hydroxides demonstrate an increase in the WF, especially in the case of CaO. One of the reasons of that interesting fact may be associated with the addition of covalency by hydroxyl anion which as discussed above may govern the intensity of the charge transfer in the hydroxides. This idea is supported by observation data that in CaO/Mo(001) system,[114] where no additional charge transfer occurs but some covalent binding may appear at the Ca−Mo interface, the WF is raised to 4.0 eV.

E. Optical properties

Using the HSE06 electronic-structure description as a starting point, computations of the optical spectra were numerically carried out within the frequency-dependent GW_0 method as implemented in VASP[56–59] in two stages: at first, the components of the dielectric matrix $\epsilon(\omega)$ were calculated in an independent-particle approach with due regard to LF effects, the accounting for which is mandatory for the proper treatment of polar semiconductors and, especially, insulators. Then G_3W_0 calculations were performed to get the energies of the single quasi-particle states. Combination of the GW approach with the numerical solution of the Bethe-Salpeter equation have been used in our previous work[116] to investigate the excitonic contributions in the optical spectra of the hydroxides.

The knowledge of single quasi-particle spectra in the hydroxides allowed us to complete a thorough work on predictions of the fundamental band gaps ranging from PBE-GGA to G_3W_0 approximation (see Table XII). Unfortunately, there are no available data on the optical spectra of $X(OH)2$ from which one would possible directly to extract the electronic band gaps. Under such circumstances, a pragmatic approach is to employ the well-known fact that in most cases, the hybrid functionals such as HSE06 and PBE0 as well as GW approximation are quantitatively predictive for ion-covalent systems. The corresponding results summarized in Table XII appear to be very similar for each compound being in a fairly narrow interval, what in turn causes us to anticipate that the experimentally determined size of the electronic band gap will very likely fall in the range of 7.7-8.3 eV for $Mg(OH)_2$ and 7.3-7.6 eV for $Ca(OH)_2$. Thus, it is seen that the $X(OH)2$ hydroxides are wide band gap insulators, which, in an ideal case, are expected to be well transparent to the visible and soft near ultraviolet ranges of electromagnetic radiation.

Table XII: Predictions of fundamental band gaps (in eV) for the bulk $Mg(OH)_2$ and $Ca(OH)_2$. As an additional test, MetaGGA calculations with the TB-mBJ potential[117,118] have been carried out (MBJ column).

Compound	PBE	HSE06m	MBJ	G_3W_0	PBE0	Expt.
$Mg(OH)_2$	3.83	7.70	7.16	8.26		7.00[a]
$Ca(OH)_2$	3.76	7.33	7.20	7.55	7.50[b]	

[a]Estimated from experimental data.34
[b]Calculated within a modified PBE0 hybrid functional[43] with the fraction of the Fock exchange taken as $a = 0.374$.[119]

Next we display in Figure 10 the calculated optical parameters of $Mg(OH)_2$ and $Ca(OH)_2$. All these quan-

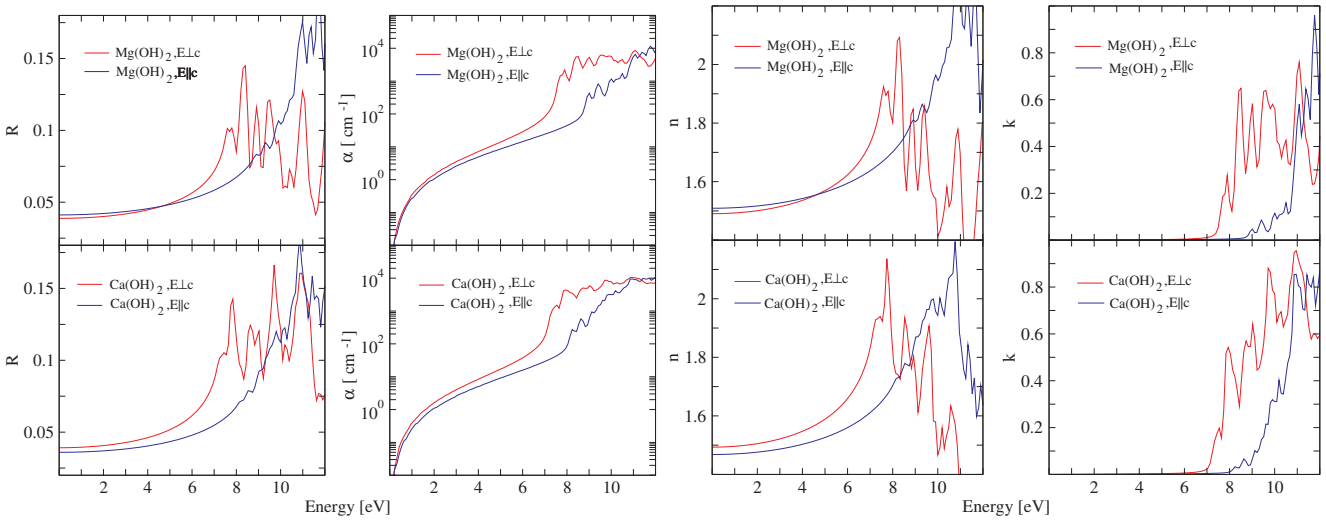

Figure 10: Optical properties of $Mg(OH)_2$ and $Ca(OH)_2$ in terms of the reflectivity $R(\omega)$, the absorption coefficient $\alpha(\omega)$, the refractive index $n(\omega)$, and the extinction coefficient $k_e(\omega)$ for the energy range from 0 to 12 eV. The quantity E denotes the electric field of the light wave which is chosen to be parallel ($E \parallel \mathbf{c}$) and perpendicular ($E \perp \mathbf{c}$) to the crystallographic $\mathbf{c}$ axes.

tities have been obtained using the known macroscopic relations composed of the real and imaginary parts of the electronic dielectric function. It is of importance to note that there is a strongly pronounced difference between the transverse and longitudinal components of the optical characteristics. In particular, the spectra for the $E \perp \mathbf{c}$ direction not only are "red-shifted" toward the CB edge by ~ 2 eV but also demonstrate larger intensities than those for $E \parallel \mathbf{c}$. At the same time, these differences are substantially smaller in the transparent region. In order to explain the effect of an anisotropy of the optical properties, which is evidently related to the diversity of the $\epsilon_\perp(\omega)$ and $\epsilon_\parallel(\omega)$ elements and presents in the both hydroxides, it could be helpful to look at the PDOS pictures in terms of the splitting of the oxygen valence states observed in Fig. 7. It is seen that the transverse component of $\Im\epsilon(\omega)$ stems from the oxygen $(2p_x, 2p_y)$ orbitals, which provide the direct band gap electric-dipole transitions starting from the fundamental absorption edge, whereas the contribution of the hybridized $2p_z$ and s orbitals becomes actual at more high exciting energies. A further point to be made is that in the self-absorption region frequency profile of the optical parameters has a rich structure, which is caused the polarization dependencies of the dipolar part of the target optical spectra and reflected in both the peak positions and their intensities. In other words, due to the lack of any noticeable d-related contributions near the fundamental absorption edge one can suggest that the anisotropy of optical properties of the hydroxides is mainly determined by electronic transitions from the three highest valence bands and governed in terms of dipolar selection rules associated with the $(2p_x, 2p_y)$ and p_z oxygen states, respectively. For higher energies in $Ca(OH)_2$, the dipole transition matrix elements will begin additionally to select Ca $3d$-related states to make thereby corrections to the polarization dependencies following from the p-type orbitals.

F. Discussion

Apart from different details of the hexagonal symmetry of the $X(OH)2$ hydroxides, the major structural feature is strictly determined by $2D$ layers of $XO6$ octahedra that are attached together by an ordered set of perpendicular O−H connections. For that reason the structural $X-O-H$ model unit was chosen in our work to describe how bonds between the atoms are cooperated to form the bulk periodic solid. Although certain structural details often are responsible for peculiar properties of a crystalline system, we have seen that the typical bonding situation in the hydroxides is strictly of anisotropic character which is governed by the strong oxygen-hydrogen binding in the hydroxyl anion. As a result, all the responses of $XO6$ octahedra appear to be direction dependent, what in turn gives rise to a planar anisotropy of physical properties of the $X(OH)2$ hydroxides. Pictorial illustrations of this fact are such macroscopic characteristic features as the significant difference of linear compressibilities along the c- and a axises (Table VI), the large degree of elastic anisotropy, or an inherent bias of optical spectra in favor of higher energies, which depends on where the electric field of the light wave is directed.

Of course, it is generally clear that such specificity of the bonding situation should hold whether $Mg(OH)_2$ or $Ca(OH)_2$ is considered. However, there still remains one interesting question connected with some signatures of a crystal field, which turn out to be mismatched between these systems: as seen from Figure 7 the splitting between the $(2p_x, 2p_y)$ and p_z oxygen subbands is much larger for $Ca(OH)_2$ than in the case of $Mg(OH)_2$, so one

can ask what might cause this discrepancy? A feasible explanation is evidently related to the higher affinity of Mg^{2+} to hydroxyl anionic groups in crystalline medium as compared with Ca^{2+}. In particular, from our results concerning structural, aggregate and vibrational properties it is seen that the $Mg^{2+}\rightarrow Ca^{2+}$ cationic substitution leads to remarkable alteration of local chemical environment in $XO6$ octahedra. For instance, the difference in affinities can be demonstrated by comparison to the Cauchy relationships[100] for a hexagonal crystal: $C_{12} = C_{66}$ and $C_{13} = C_{44}$. The theoretically calculated values of the ratios C_{12}/C_{66} and C_{13}/C_{44} for $Ca(OH)_2$, 0.89 and 0.86, respectively, are much closer to unity than those, 0.81 and 0.46, for $Mg(OH)_2$. It therefore appears that the structural role of Ca^{2+} cation in the interatomic potential of $Ca(OH)_2$ is mainly associated with central nearest-neighbor forces,[100] while the effect of the Mg^{2+} cation in $Mg(OH)_2$ is more complex since cannot be definitely reduced to two-body interactions.

The other important aspect our results give is an understanding how via varying complexity of the chemical bonds one can control macroscopic properties of materials. In particular, as compared with the simple oxides the key feature of the bonding picture in the hydroxides, which is mainly essential in materials context, is the regulation of the charge transfer degree by the bridging oxygen anion. On the one hand, it is just the case why $X(OH)2$ is less mechanically stable than their binary XO prototypes. However, on the other hand, it would be of even greater importance to emphasize that this could be the main factor for getting the desired electronic and optical properties.

IV. CONCLUSION

This work presents a study of materials properties for $X(OH)2$ (X=Mg and Ca) by first-principles calculations by employing state-of-art (HSE06, GW) DFT methods. We have focused on the ground state properties, electronic structure and optical properties. Analysis of the overall bonding picture has shown that a crystal-chemical integrity of the hydroxides is governed by the oxygen via a bridging combination of the strong covalent bonding in the hydroxyl anion and the metal-oxygen ionic connection. This feature is a principal component of the multifunctionality of $X(OH)2$ compounds because it provides the equal utilization of electronic characteristics such as large band gap and low refractive index (relevant to purely ionic systems) and the covalent contributions from the oxygen. We show that $X(OH)2$ has a direct band gap with the VB and CB extreme at the Γ point. Predictions for the fundamental band gaps were shown to be in the range of 7.7-8.3 eV for $Mg(OH)_2$ and 7.3-7.6 eV for $Ca(OH)_2$. The bottommost CB is well dispersive, whereas the topmost VB is almost dispersionless. Effective masses of carriers in vicinity of the band extreme are strongly anisotropic, and for the electrons are similar to those in ZnO. Optical properties of the bulk crystalline $X(OH)2$ hydroxides have been studied by using the many-body Hedin's GW approximation. The results indicate a weak absorption of electromagnetic radiation with photon energies near the fundamental band gap, which is in agreement with subsequent optical studies. The potential of applicability of the $X(OH)2$ compounds in semiconductor device engineering and optoelectronics is discussed.

Acknowledgments

This work has received financial and supercomputing support from the Research Council of Norway within the FME project (192839) and ISP NANOMAT project (181884) as well as by the European Union through the European Regional Development Fund (Centre of Excellence "Mesosystems: Theory and Applications", TK114) and by the Estonian Science Foundation (grant No 7296).

* Electronic address: smagulk@ife.no

[1] T. Krüger, *Sequestering carbon dioxide from the atmosphere by enhancing the capacity of the oceans to act as a carbon sink* (2008).
[2] C. Estrela, F. C. Pimenta, I. Y. Ito, and L. L. Bammann, J. Endod. **24**, 15 (1998).
[3] Electroch. Acta **100**, 85 (2013).
[4] Q. Cao, F. Huang, Z. Zhuang, and Z. Lin, Nanoscale **4**, 2423 (2012).
[5] A. Gibson and M. Maniocha, Martin Marietta Magnesia Specialties, LLC pp. 1–7 (2004).
[6] E. Ghali, W. Dietzel, and K.-U. Kainer, J. Mater. Eng. Perform. **13**, 7 (2004).
[7] A. C. Snider, Mat. Res. Soc. Symp. Proc. **757**, II8.3.1 (2003).
[8] H. Dhaouadi, H. Chaabane, and T. Fathi, Nano-Micro Lett. **3**, 153 (2011).
[9] C. Henrist, J.-P. Mathieu, C. Vogels, A. Rulmont, and R. Cloots, J. Cryst. Growth **249**, 321 (2003).
[10] J. Jan and J. Kuera, Polym. Eng. Sci. **30**, 707713 (1990).
[11] L. Shi, D. Li, J. Wang, S. Li, D. G. Evans, and X. Duan, Clays Clay Miner. **53**, 294 (2005).
[12] C.-H. Huang, Y.-L. Jan, and W.-C. Lee, J. Electrochem. Soc. **158**, H879 (2011).
[13] H. Miyazaki, R. Mikami, A. Yamada, and M. Konagai, Jpn. J. Appl. Phys., Part 1 **45**, 2618 (2006).
[14] Y. Zhu, Q. Zhao, Y.-H. Zhang, and G. Wu, Surf. Coat. Technol. **206**, 2961 (2012).
[15] P. Wang, C. Li, H. Gong, H. Wang, and J. Liu, Ceram. Int. **37**, 3365 (2011).
[16] A. K. Mukhopadhyay, P. S. Das, A. Dey, M. Raychaudhuri, A. K. Mandal, and N. Dey, J. Inst. Eng. (India):

Series D **93**, 53 (2012).
[17] D. An, X. Ding, Z. Wang, and Y. Liu, Colloids Surf. A **356**, 28 (2010).
[18] T. Kuji, M. Chiba, T. Honjo, and K. Kotoda, *Patent TW200923974. Transparent conductive film and method for making same* (2009).
[19] T. Honjo, M. Chiba, and T. Kuji, eJ. Surf. Sci. Nanotechnol. **7**, 791 (2009).
[20] S. Z. Karazhanov, in *International Conference on Nanomaterials and Nanocomposites Synthesis, Properties and Applications*, edited by M. Umadevi and R. Parimaladevi, Department of Physics, Mother Teresa Womens University, Kodaikanal, Tamilnadu, India (Excel India Publishers, New Delhi, 2013), pp. 6–10.
[21] T. A. N. Peiris, S. Senthilarasu, and K. G. U. Wijayantha, J. Phys. Chem. C **116**, 1211 (2012).
[22] T. A. Nirmal Peiris, K. G. Upul Wijayantha, and J. Garcia-Canadas, Phys. Chem. Chem. Phys. **16**, 2912 (2014).
[23] J.-H. Yum, S. Nakade, D.-Y. Kim, and S. Yanagida, J. Phys. Chem. B **110**, 3215 (2006).
[24] D. E. Haycock, M. Kasrai, C. J. Nicholls, and D. S. Urch, J. Chem. Soc., Dalton Trans. pp. 1791–1796 (1978).
[25] Y. Zhu, G. Wu, Y.-H. Zhang, and Q. Zhao, Appl. Surf. Sci. **257**, 6129 (2011).
[26] K. Azuma, T. Oda, and S. Tanaka, Comput. Theor. Chem. **963**, 215 (2011).
[27] P. Baranek, A. Lichanot, R. Orlando, and R. Dovesi, Chem. Phys. Lett. **340**, 362 (2001).
[28] B. Weckler and H. D. Lutz, Spectrochim. Acta, Part A **52**, 1507 (1996).
[29] H. D. Lutz, H. Müller, and M. Schmidt, J. Mol. Struct. **328**, 121 (1994).
[30] J. C. Owrutsky, N. H. Rosenbaum, L. M. Tack, and R. J. Saykally, J. Chem.l Phys. **83**, 5338 (1985).
[31] R. L. Frost and J. T. Kloprogge, Spectrochim. Acta, Part A **55**, 2195 (1999).
[32] B. Winkler, V. Milman, B. Hennion, M. C. Payne, M. H. Lee, and J. S. Lin, Phys. Chem. Miner. **22**, 461 (1995).
[33] P. S. Braterman and R. T. Cygan, Am. Mineral. **91**, 1188 (2006).
[34] T. Murakami, T. Honjo, and T. Kuji, Mater. Trans. **52**, 1689 (2011).
[35] L. Hedin, Phys. Rev. **139**, A796 (1965).
[36] J. Heyd, G. E. Scuseria, and M. Ernzerhof, J. Chem. Phys. **118**, 8207 (2003).
[37] A. V. Krukau, O. A. Vydrov, A. F. Izmaylov, and G. E. Scuseria, J. Chem. Phys. **125**, 224106 (2006).
[38] T. M. Henderson, J. Paier, and G. E. Scuseria, Phys. Status Solidi B **248**, 767 (2011), ISSN 1521-3951.
[39] J. Vidal, S. Botti, P. Olsson, J. F. Guillemoles, and L. Reining, Phys. Rev. Lett. **104**, 056401 (2010).
[40] S. Botti and J. Vidal, *Energy Generation: Solar Energy* (John Wiley & Sons Ltd, 2013), book section 2, pp. 29–69, Computational Approaches to Energy Materials.
[41] A. Alkauskas, P. Broqvist, F. Devynck, and A. Pasquarello, Phys. Rev. Lett. **101**, 106802 (2008).
[42] A. Alkauskas, P. Broqvist, and A. Pasquarello, Phys. Status Solidi B **248**, 775 (2011).
[43] M. A. L. Marques, J. Vidal, M. J. T. Oliveira, L. Reining, and S. Botti, Phys. Rev. B **83**, 035119 (2011).
[44] J. He and C. Franchini, Phys. Rev. B **86**, 235117 (2012).
[45] J. E. Moussa, P. A. Schultz, and J. R. Chelikowsky, J. Chem. Phys. **136**, 204117 (2012).
[46] G. Kresse and J. Furthmüller, Phys. Rev. B **54**, 11169 (1996).
[47] P. E. Blöchl, Phys. Rev. B **50**, 17953 (1994).
[48] G. Kresse and D. Joubert, Phys. Rev. B **59**, 1758 (1999).
[49] G. Kresse and J. Hafner, Phys. Rev. B **47**, 558 (1993).
[50] J. P. Perdew, K. Burke, and M. Ernzerhof, Phys. Rev. Lett. **77**, 3865 (1996).
[51] M. Gajdoš, K. Hummer, G. Kresse, J. Furthmüller, and F. Bechstedt, Phys. Rev. B **73**, 045112 (2006).
[52] A. Schleife, C. Rödl, F. Fuchs, J. Furthmüller, and F. Bechstedt, Phys. Rev. B **80**, 035112 (2009).
[53] A. Schleife, C. Rdl, J. Furthmller, and F. Bechstedt, New J. Phys. **13**, 085012 (2011).
[54] A. Schleife and F. Bechstedt, J. Mater. Res. **27**, 2180 (2012).
[55] G. Cappellini, J. Furthmüller, E. Cadelano, and F. Bechstedt, Phys. Rev. B **87**, 075203 (2013).
[56] M. Shishkin and G. Kresse, Phys. Rev. B **74**, 035101 (2006).
[57] M. Shishkin and G. Kresse, Phys. Rev. B **75**, 235102 (2007).
[58] F. Fuchs, J. Furthmüller, F. Bechstedt, M. Shishkin, and G. Kresse, Phys. Rev. B **76**, 115109 (2007).
[59] M. Shishkin, M. Marsman, and G. Kresse, Phys. Rev. Lett. **99**, 246403 (2007).
[60] S. Z. Karazhanov, P. Ravindran, A. Kjekshus, H. Fjellvåg, and B. G. Svensson, Phys. Rev. B **75**, 155104 (2007).
[61] P. Ravindran, A. Delin, B. Johansson, O. Eriksson, and J. M. Wills, Phys. Rev. B **59**, 1776 (1999).
[62] L. Desgranges, G. Calvarin, and G. Chevrier, Acta Crystallogr., Sect. B: Struct. Sci. **52**, 82 (1996).
[63] M. Catti, G. Ferraris, S. Hull, and A. Pavese, Phys. Chem. Miner. **22**, 200 (1995).
[64] L. Desgranges, D. Grebille, G. Calvarin, G. Chevrier, N. Floquet, and J.-C. Niepce, Acta Crystallogr., Sect. B: Struct. Sci. **49**, 812 (1993).
[65] W. R. Busing and H. A. Levy, J. Chem. Phys. **26**, 563 (1957).
[66] H. Oswald and R. Asper, in *Preparation and Crystal Growth of Materials with Layered Structures*, edited by R. M. A. Lieth (Springer, 1977), vol. I of *Physics and Chemistry of Materials with Layered Structures*, pp. 71–140.
[67] F. Freund, vol. 2 of *Chem. Solid State Mater.* (Cambridge University Press, 1992).
[68] P. Ugliengo, F. Pascale, M. Mérawa, P. Labéguerie, S. Tosoni, and R. Dovesi, J. Phys. Chem. B **108**, 13632 (2004).
[69] P. Fabien, T. Sergio, Z.-W. Claudio, U. Piero, O. Roberto, and D. Roberto, Chem. Phys. Lett. **396**, 308 (2004).
[70] P. Ugliengo, C. M. Zicovich-Wilson, S. Tosoni, and B. Civalleri, J. Mater. Chem. **19**, 2564 (2009).
[71] P. T. Jochym, A. M. Oleś, K. Parlinski, J. Łażewski, P. Piekarz, and M. Sternik, J. Phys.: Condens. Matter **22**, 445403 (2010).
[72] Y. Hase, J. Brazilian Chem. Soc. **17**, 741 (2006).
[73] P. Dawson, C. D. Hadfield, and G. Wilkinson, J. Phys. Chem. Solids **34**, 1217 (1973).
[74] Z. Padanyi, Solid State Commun. **8**, 541 (1970).
[75] B. A. Phillips and W. R. Busing, J. Phys. Chem. **61**, 502 (1957).
[76] T. Kamisuki and S. Maeda, Bull. Chem. Soc. Jpn. **45**, 1345 (1972).
[77] R. Krishnan, *Prog. Cryst. Phys.* (S. Viswanathan, 1958).

[78] M. E. Gurtin, in *Handbuch der Physik*, edited by S. Flügge and C. Truesdell (Springer, 1972), book section 1, pp. 1–295.
[79] X. Xia, D. J. Weidner, and H. Zhao, Am. Mineral. **83**, 68 (1998).
[80] F. Jiang, S. Speziale, and T. S. Duffy, Am. Mineral. **91**, 1893 (2006).
[81] F. Holuj, M. Drozdowski, and M. Czajkowski, Solid State Commun. **56**, 1019 (1985).
[82] R. A. Cowley, Phys. Rev. B **13**, 4877 (1976).
[83] R. W. Terhune, T. Kushida, and G. W. Ford, Phys. Rev. B **32**, 8416 (1985).
[84] R. Hill, Proc. Phys. Soc. Sect A **65**, 349 (1952).
[85] T. S. Duffy, T. J. Ahrens, and M. A. Lange, J. Geophys. Research: Solid Earth **96**, 14319 (1991).
[86] Y. Fei and H.-K. Mao, J. Geophys. Research: Solid Earth **98**, 11875 (1993).
[87] J. B. Parise, K. Leinenweber, D. J. Weidnner, K. Tan, and R. B. Von Dreele, Am. Mineral. **79**, 193 (1994).
[88] C. Meade and R. Jeanloz, Geophys. Research Lett. **17**, 1157 (1990).
[89] A. Pavese, M. Catti, G. Ferraris, and S. Hull, Phys. Chem. Miner. **24**, 85 (1997).
[90] H. Reichmann, S. Speziale, C. Lathe, M. Wehber, and F. Schilling, *High P - study of Portlandite* (DESY Photon Science, HAMBURG, 2007).
[91] H. Ding, W. Chen, and L. Zhang, *Elasticity of Transversely Isotropic Materials*, Solid Mechanics and Its Applications (Springer, 2006).
[92] S. T. P. of Chemical Substances, in *CRC Handbook of Chemistry and Physics, 85th Edition*, edited by D. Lide (2004).
[93] M. Winter, *Web elements: the periodic table on the www* (1993-2011), URL `http://www.webelements.com/`.
[94] D. L. Anderson and O. L. Anderson, J. Geophys. Res. **75**, 3494 (1970).
[95] N. N. Kristoffel, Czech. J. Phys. B **34**, 1253 (1984).
[96] N. Kristoffel and K. P., Phys. Status Solidi (B) **149**, 11 (1988).
[97] A. Bussmann-Holder, H. Bilz, and G. Benedek, Phys. Rev. B **39**, 9214 (1989).
[98] A. Pishtshev, Phys. B **406**, 1586 (2011).
[99] K.-W. Lee and W. E. Pickett, Phys. Rev. B **68**, 085308 (2003).
[100] M. Born and K. Huang, *Dynamical Theory of Crystal Lattices*, International series of monographs on physics (Clarendon Press, 1954).
[101] F. Freund, Fortschr. chem. Forsch. **10**, 347 (1968).
[102] F. Freund and D. Sornette, Tectonophys. **431**, 33 (2007).
[103] F. A. Francis A. Carey and R. M. Giuliano (McGraw-Hill, 2010).
[104] K. Hümmer, Phys. Status Solidi **B 56**, 249 (1973).
[105] W. R. L. Lambrecht, A. V. Rodina, S. Limpijumnong, B. Segall, and B. K. Meyer, Phys. Rev. B **65**, 07 5207 (2002).
[106] S. Z. Karazhanov, P. Ravindran, U. Grossner, A. Kjekshus, H. Fjellvåg, and B. G. Svensson, J. Appl. Phys. **100**, 043709 (2006).
[107] D. E. Haycock, M. Kasrai, C. J. Nicholls, and D. S. Urch, J. Chem. Soc., Dalton Trans. pp. 1791–1796 (1978).
[108] A. Subrahmanyam and S. Kumar, *The Kelvin Probe for Surface Engineering: Fundamentals and Design* (CRC Press, New Delhi, Chennai, Mumbai, Bengaluru, Kolkata, Thiruvananthapuram, Lucknow, 2010).
[109] R. A. Marcus, Rev. Mod. Phys. **65**, 599 (1993).
[110] C. J. Fall, N. Binggeli, and A. Baldereschi, J. Phys.: Condens. Matter **11**, 2689 (1999).
[111] J. J. Attema, M. A. Uijttewaal, G. A. de Wijs, and R. A. de Groot, Phys. Rev. B **77**, 165109 (2008).
[112] A. Slepko, A. A. Demkov, W. Y. Loh, P. Majhi, and G. Bersuker, J. Appl. Phys. **109**, 083703 (2011).
[113] G. Samsonov, *The Oxide Handbook*, IFI Data Base Library (IFI/Plenum, 1982).
[114] X. Shao, Y. Cui, W.-D. Schneider, N. Nilius, and H.-J. Freund, J. Phys. Chem. C **116**, 17980 (2012).
[115] S. Kikuchi, Y. Takahashi, and T. Sakata, Appl. Opt. **8**, 42 (1969).
[116] Pishtshev, A., Karazhanov, S. Zh., and Klopov, M., Phys. Rev. B p. submitted (2014).
[117] F. Tran and P. Blaha, Phys. Rev. Lett. **102**, 226401 (2009).
[118] D. Koller, F. Tran, and P. Blaha, Phys. Rev. B **83**, 195134 (2011).
[119] A. Pishtshev and M. Klopov, in *Abstr. Int. Conf. on Functional Materials and Nanotechnologies 2012*, edited by A. Sternbergs and L. Grinberga (University of Latvia, Riga, 2012), p. 117.
[120] V. V. Brazhkin, A. G. Lyapin, and R. J. Hemley, Phil. Mag. A **82**, 231 (2002).
[121] this value was estimated via the shear modulus according to Ref. [120].

Graphical abstract

A. Pishtshev, S. Zh. Karazhanov, and M. Klopov

By means of the base of first-principle calculations the global stability of the crystalline structure of magnesium and calcium hydroxides was proved. Mechanical "softness" of $Ca(OH)_2$ crystalline hydroxide was demonstrated. Crystal-chemical integrity of the hydroxides is controlled by the oxygen via a bridging combination of the strong covalent bonding in the hydroxyl anion and the metal-oxygen ionic connection. Crystalline stability of the hydroxides is closely connected with the character of non-bonding valence lone-pairs distribution in the hydroxyl anion. On the base of the calculated electronic structure the strong anisotropy of optical properties have been predicted.